Classifying Craniosynostosis with a 3D Projection-Based Feature Extraction System

Irma Lam*, Michael Cunningham†, Matthew Speltz†, Linda Shapiro‡

*Dept. of Biomedical Informatics and Medical Education, University of Washington, Seattle, WA 98195, USA
†Seattle Children's Research Institute, Seattle, Washington 98101, USA
‡Dept. of Computer Science & Engineering, University of Washington, Seattle, WA 98195, USA

E-mail: {irmalam@u, shapiro@cs}.washington.edu
{michael.cunningham, matt.speltz}@seattlechildrens.org

***Abstract*—Craniosynostosis, a disorder in which one or more fibrous joints of the skull fuse prematurely, causes skull deformity and is associated with increased intracranial pressure and developmental delays. Although clinicians can easily diagnose craniosynostosis and can classify its type, being able to quantify the condition is an important problem in craniofacial research. While several papers have attempted this quantification through statistical models, the methods have not been intuitive to biomedical researchers and clinicians who want to use them. The goal of this work was to develop a general platform upon which new quantification measures could be developed and tested. The features reported in this paper were developed as basic shape measures, both single-valued and vector-valued, that are extracted from a single plane projection of the 3D skull. This technique allows us to process images that would otherwise be eliminated in previous systems due to poor resolution, noise or imperfections on their CT scans. We test our new features on classification tasks and also compare their performance to previous research. In spite of its simplicity, the classification accuracy of our new features is significantly higher than previous results on head CT scan data from the same research studies.**

I. Introduction

Craniosynostosis is a birth defect that occurs when one or more sutures, the fibrous joints of the skull, fuse prematurely [1]. Despite the prevalence of this condition, the natural course of craniosynostosis is not well understood. An infant's skull is made up of several bony plates (calvaria), connected by sutures. The persistence of sutures between the calvaria is necessary for skull deformation during birth and expansion of the cranial vault during brain growth. The four main sutures of the calvarial vault are the sagittal suture, left and right coronal sutures, metopic suture, and left and right lambdoid sutures. The sutures must remain unossified so that the skull can stay malleable and the brain can have enough space to grow properly. Most craniosynostosis cases are isolated, with only one fibrous suture on an infant's skull fusing prematurely, but there are also syndromic cases with multiple affected sutures. A skull cannot easily expand perpendicular to a closed suture, which redirects growth parallel to the closed suture. Subsequently, a misshapen head and frequently abnormal facial features are induced [2].

Craniosynostosis occurs in one in 2,000 to 2,500 live births [1]. Sagittal synostosis, the most common form, represents about 40% to 55% of the non-syndromic cases. Coronal synostosis, the second most common synostosis, represents about 20% to 25%. Metopic synostosis, the third most common synostosis, represents about 5% to 15%. Each class shape (sagittal, unilateral coronal and metopic) is illustrated in Fig. 1. If left untreated, craniosynostosis can be associated with increasing intracranial pressure [3] and neurocognitive delays.

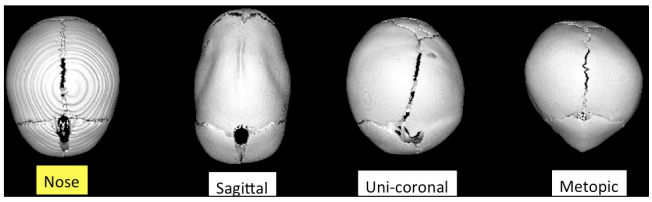

Fig. 1. Shapes of unaffected (left), sagittal, uni-coronal and metopic synostosis skulls.

Currently, the diagnosis of craniosynostosis relies on clinical evaluation by a trained clinician. If synostosis is suspected, a CT scan of the head may be ordered as part of a standard diagnostic procedure. Sometimes the deformity caused by craniosynostosis may be mild at birth, and the signs can take a few months to become visually noticeable; however, early detection is essential to a timely surgery, while the infant is experiencing rapid brain growth. The objective of the surgery is to allow cranial expansion so that there will be adequate space for the brain to grow, intracranial pressure can be prevented and a normal appearance of the child's head can be restored. Although clinicians can easily diagnose craniosynostosis and can classify its type, being able to quantify the condition is an important problem in craniofacial research. The goal of this work was to develop a general platform upon which new quantification measures could be developed and tested on large numbers of CT subject images from multiple different sites and CT setup environments.

The rest of the paper is organized as follows. Section II discusses the related work. Section III describes the data set used in this study. Section IV presents the approach and methodology that are used in our system to process,

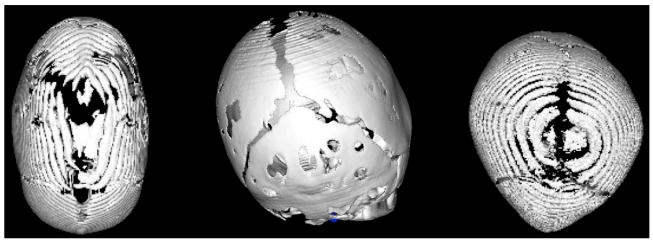

Fig. 2. Imperfections like holes, rings and noise as seen on some older CT scans can make processing and shape analysis difficult.

extract important information, analyze and classify the data. Section V presents the classification results using our image processing and analytic system. Finally, Section VI provides the conclusions.

II. Related Work

A. Various Representative Descriptors

Ruiz-Correa *et al.* [4] developed the cranial image, a high-dimensional distance matrix representation of the skull, and used it to classify different types of craniosynostosis. Lin *et al.* [5] extended the methodology to symbolic-signature descriptors derived from the cranial image. With the symbolic descriptors capturing the information in the much larger cranial image, Lin obtained a more compact representation of a 3D shape. The symbolic shape descriptors encode global geometric properties that capture the uniqueness of each shape class by probabilistic modeling of their local geometric properties.

Atmosukarto *et al.* [6] determined several measures for quantifying the severity of deformational plagiocephaly (DP), a postnatal flattening of the back of the skull. Her descriptors used the concept of an azimuth-elevation-angle histogram of the surface normals of the back of the head and produced severity errors that were functions of the left and right side bins of these histograms. Atmosukarto's approach achieved high accuracy (all classification were greater than 90%) in distinguishing DP cases from non-DP controls. Her *asymmetry score* descriptor provided the best overall discrimination.

Lele and Richtsmeier [7] have used descriptors that combined *Euclidian distance matrix analysis* (EDMA) and likelihood-based classification methods but the approach led to a high error rate in the 18 – 32% range, as discussed in Ruiz-Correa [8].

B. Sparse Logistic Regression Models

Yang et al. [9] developed a plane-based retrieval system that produced a variation of Ruiz-Correa's cranial image. To classify, Yang used logistic regression, L_1-regularized logistic regression, the fused lasso and the clustering lasso classifiers but the method requires a high-dimensional 100 x 100 distance matrix to achieve mid-90% classification accuracy. Yang traded higher computational and memory costs for better performance. Her method was also sensitive to poor resolution, noise or other imperfections on the original CT scans, as shown in Fig. 2; consequently, only 70 skull images could be used. Furthermore, some automatically-placed landmark points were not correct.

Our work builds on the work of Yang, but there are important differences. Our methods were able to process additional data including 149 total skull images of four different types: sagittal, unilateral coronal, metopic, and control. Yang had less data and no control images. Yang's features were simply a set of points taken along the contour of the skull on multiple different planes. We have developed specific shape descriptors for our work. Finally, because Yang had no controls, her experiments could only classify abnormals compared to other abnormals. We are able to classify abnormals as compared to controls, which is the more medically relevant task when it is used for diagnosis, as well as to compare our work to Yang's by making the same two-class comparisons and multi-class comparisons she made.

C. Classifying by Inspection

In some clinics, visual inspection was highly encouraged. For example, in Massimi's clinics [10], CT scans were restricted to severe bone constriction and hypertrophic scalp veins or evident sellar deformation of the cranial vault. However, visual inspection is subjective and may be biased and limiting. Since procedures and test results that are consistent, efficient and reproducible are highly valued, developing an automated, 3D image-processing-based system for the characterization of craniosynotosis remains a research objective.

III. Data Set

For our craniosynostosis study, the 3D computed tomography (CT) scans of heads were collected from hospitals in four different cities in the US. Our study is limited to three types of synostosis: sagittal (the affected suture is between the parietal bones), metopic (the affected suture is between the frontal bones) and unilateral coronal (the affected suture is between the frontal and the parietal bones on either the right side or the left side of the skull). For the control dataset, the Radiology database at Seattle Children's Hospital was interrogated for children that had head CTs at age 2 years and younger. First, all children with craniofacial malformations, including craniosynostosis, were excluded. Next, CT scans obtained for minor head trauma, headache, or other reasons that would not effect calvarial shape were reviewed in 3D format. Finally, cases without abnormalities in calvarial form were used as controls. For our experiments, 149 skull meshes were included. 34 images were from the unaffected subjects (children who do not have craniosynostosis disorder), and 115 images were from the affected subjects (children with sagittal synostosis, unilateral coronal synostosis, or metopic synostosis). All the subjects were under two years of age.

IV. Approach and Methodology

As shown in Fig. 3, our system is a general platform for 3D craniofacial shape analysis. For this manuscript, we describe five modules:

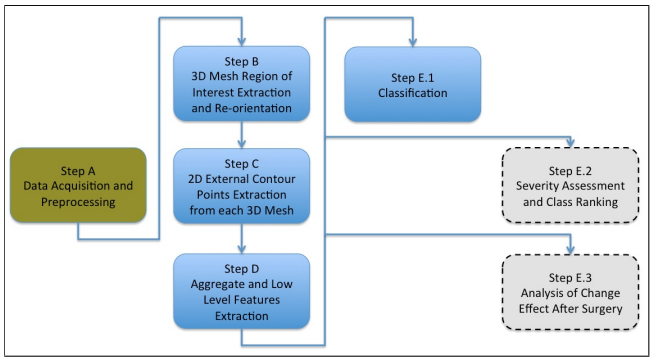

Fig. 3. Flow chart of our system. Step A *Data Acquisition and Preprocessing* is not part of the automated system being developed. Step E.2 *Severity Assessment and Class Ranking* and Step E.3 *Analysis of Change Effect After Surgery* are out of scope on this paper.

A. Data Acquisition and Preprocessing
B. 3D Mesh Region of Interest Extraction and Re-orientation
C. 2D External Contour Points Extraction from each 3D Mesh
D. Aggregate and Low Level Features Extraction
E. Classification

A. Data Acquisition and Preprocessing

This module is not part of the automated system being developed and requires human interaction.

a) CT Acquisition: Seattle Children's Hospital acquired the CT images from four different sites: Atlanta, Chicago, Seattle and St. Louis. Seattle Children's Hospital used a GE Lightspeed VCT 64-channel CT, to simultaneously obtain up to 64 slices of images from each head scan. Each slice is 0.5-mm thick with a scanning resolution of either 0.351 mm or 0.391 mm in both x and y dimensions. The sampling frequency for the scan is 2,460 Hz. Each CT image slice is stored in 16-bit and 500 x 500 pixel resolution according to the Digital Imaging and Communications in Medicine (DICOM) standard.

b) CT Cleaning: Each CT image is cleaned so that all surfaces below the chin (e.g., the neck, shoulder, clothing or hands) are deleted. We do not repair the surface or apply any smoothing algorithm to the cleaned CT image.

c) Mesh Extraction: From the CT volume data of the head, our system first extracts the skull slices and creates a single 3D image of the skull surface mesh. Each mesh contains between 140,000 and 850,000 vertices.

d) Mesh Normalization: Because our 3D CT scans are not consistently posed, our system next performs normalization on the cleaned skull surface mesh to ensure the skull poses are symmetrical between its left and right sides. For our analysis and classification, it is also important that all skull surface meshes use the same coordinate reference and orientation (top view of the skull with head facing straight and forward).

e) Landmarking: The final step in this module is landmarking, which locates and records the x-y-z locations of two landmark points: nasion and opisthion. We use only two landmark points to define our base plane. To assure consistency, the open source application meshlab is used to mark these two points by hand on each 3D surface mesh. The x-y-z location values of these two points are then stored in a text file so that the points can be used to extract the ROI and contour points for data analysis and classification. Yang's automatic landmark finder is available for future experiments.

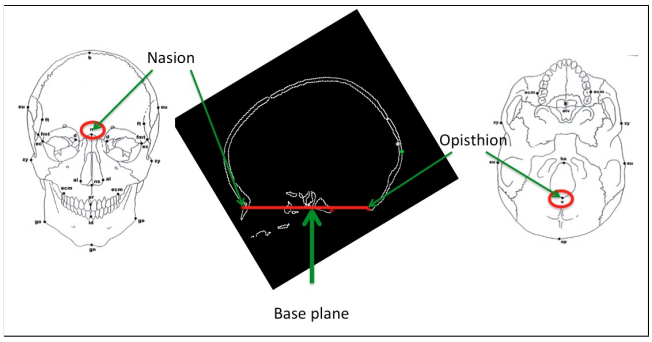

Fig. 4. Identifying the base plane based on the nasion and opisthion anatomical landmark points. This base plane was used as one x-y-z coordinate plane to re-orient the entire extracted 3D ROI.

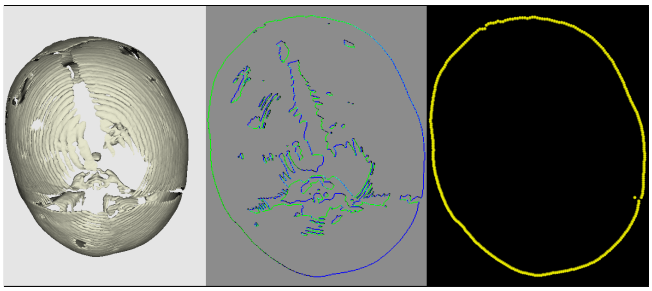

Fig. 5. Extracting a 2D external contour (right) by first projecting the 3D surface mesh (left) onto a 2D plane (middle). Keeping only the exterior points from the silhouette. This approach allows processing and shape analysis to be done even on older CT scans that have noise and challenging imperfections.

B. 3D Mesh Region of Interest Extraction and Re-orientation

Based on the location of the nasion and opisthion landmark points, the algorithm identifies a base plane as shown in Fig. 4. The surface mesh on and above this base plane is considered to be the region of interest (ROI), which our algorithm extracts and uses for the remaining analysis. This tilted base plane replaces one of the three x-y-z coordinate planes (in our case, the new z-plane). Subsequently, the coordinate reference of the 3D ROI is re-oriented. This module standardizes and positions the extracted ROI uniformly to ensure accurate comparison and later analysis.

C. 2D External Contour Points Extraction from each 3D Mesh

The bird's-eye view from the top of a skull can reveal many unique characteristics for describing its shape. Our shape analytic system uses a simple 3D projection-based contouring technique to extract exterior shape information from the 3D surface mesh as a whole. Our contour extraction module first projects a top view of the 3D ROI onto a 2D plane. Then

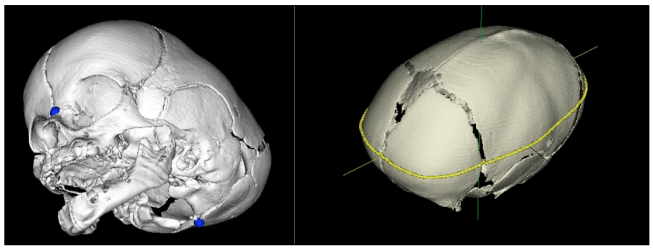

Fig. 6. Original image (left). Removing all vertices below the base plane to obtain the extracted ROI (right). The contour (yellow line on right) is rescaled and translated so that it shares the same center and bounds as the ROI.

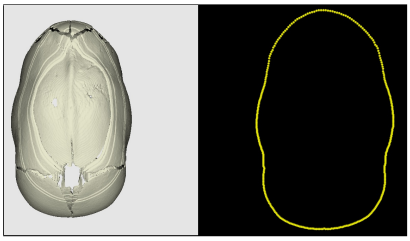

Fig. 7. A less circular skull.

it extracts only the exterior contour points uniformly in one-degree steps for a 360-degree sweep. The top view of a 3D extracted ROI and its 2D external contour are shown in Fig. 5. The contour is rescaled and translated so that it shares the same center and bounds as the extracted ROI, as shown in Fig. 6. Different numbers of contour points were experimented with by varying the degree interval, but no significant differences were observed in their resulting classification performance.

D. Aggregate and Low-Level Feature Extraction

Let the 2D contour be defined with an x-y axis, whose origin is at the center of the shape. Let P = (p_1, p_2, …, p_{360}) be the $N = 360$ contour points used to generate the features.

Our system uses two kinds of features: 1) low-level features that are computed directly from the contour points and 2) aggregate features that combine multiple low-level features mathematically to produce a single score value.

Compare to Circle is a single-valued descriptor, which compares the 2D contour to the shape of a circle. A higher error score value indicates a less circular skull, as illustrated in Fig. 7, which is less circular. A more circular skull is shown in Fig. 8. In order to avoid errors induced by skull size in this aggregate measure, size normalization is used. Otherwise, a CT scan that was acquired from an older child, whose skull might be larger would be incorrectly scored with a higher error value.

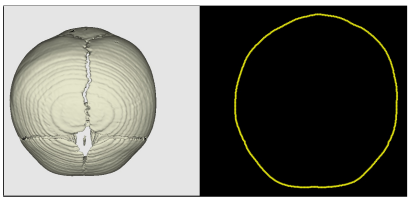

Fig. 8. A more circular skull.

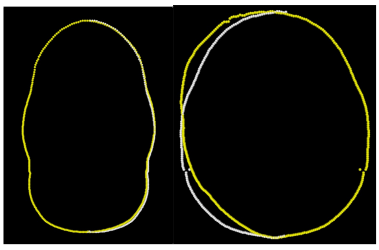

Fig. 9. Illustration of a symmetrical sagittal synostosis skull (left) and an asymmetrical unilateral coronal synostosis skull (right).

Let r_{max} be the maximum distance from origin to a point p $\in$ P and r_{min} be the minimum distance. The average distance r_{avg} is used to construct a circle centered at the origin. Then, the normalized feature *cmp2Circle* is defined by (1)

$$cmp2Circle = \frac{\sum_{p \in P} \|p_{dist} - r_{avg}\|^2}{N \times r_{avg}}. \quad (1)$$

Symmetry is a single-valued descriptor, which compares the contour points of the left and right sides to determine the symmetry of a skull. A higher error score value indicates a more asymmetrical skull. As shown in Fig. 9, our algorithm divides the contour into left and right sides. The yellow lines represent the complete contour extracted from both sides of a skull. The white lines are the mirror image from one side, flipped to the opposite side so that the symmetrical characteristic of a skull can be easily visualized. If the yellow and white lines meet exactly, the skull is perfectly symmetrical. For example, the unilateral coronal skull on the right side in Fig. 9 shows a highly asymmetrical characteristic. The side where the white line lies is the side our algorithm determines to have an affected suture.

Let P_R = (pr_1, pr_2, …, pr_n, …, pr_{180}) be the 180 points on the right side of the contour, P_L = (pl_1, pl_2, …, pl_n, …, pl_{180}) be those on the corresponding left side.

Let $pr_n = (x, y)$ and its corresponding point $pl_n = (a, b)$. Let pl'_n be the mirror image of pl_n along the y-axis. With origin at $(0, 0)$, $pl'_n = (-a, b)$. The Euclidean distance $d(pr_n, pl'_n) = \sqrt{(x+a)^2 + (y-b)^2}$. Then, the normalized feature *symmetry* is defined by (2)

$$symmetry = \frac{\sum_{pr \in P_R, pl \in P_L} d(pr, pl')}{N \times r_{avg}}. \quad (2)$$

Angle is a low-level vector descriptor, which describes the angle between a line with the slope of two neighboring contour points and the horizontal x-axis. In our experiments, there are 360 contour points. Therefore, there are 180 angle descriptor features on the front side of the skull contour, and there are another 180 on the back.

This feature is a 360-dimensional vector whose values are computed at each pair of consecutive contour points. For such a pair (p_i, p_j), the angle is given by the arctangent as in (3)

$$angle = \arctan(\frac{y_j - y_i}{x_j - x_i}) \times \frac{180^\circ}{\pi}. \quad (3)$$

Radius Distance is a low-level vector descriptor, which describes the radius distance from each contour point to the center of the extracted surface mesh. There are a total of 360 contour points, one degree apart. Therefore, there are a total of 180 radius distance descriptor features on the front side of the skull contour, and there are another 180 on the back.

This feature is a 360-dimensional vector whose values are computed at each contour point. For a point p_i, the distance is given by its distance to the origin $(0, 0)$ as in (4)

$$dist(p_i) = \|p_i\|^2. \quad (4)$$

E. Classification

In the *Classification* module, sequential minimal optimization (SMO) and logistic regression, both of which are linear classifiers that assign a score to predict class are used from the WEKA suite of classifiers. The SMO classifier is essentially a support vector machine. In general, 10-fold cross-validation experiments are applied to evaluate the performance of the trained classifiers, except when comparing to previous results that used 3-fold cross-validation. Each experiment is run several times by randomizing the incidents in order to observe any unexpected outliers, unusual patterns or unexplainable randomness in the results. Prediction accuracy is recorded.

V. Experiments and Results

In our classification experiments, there were three affected skull datasets: a 57 subject sagittal dataset, a 33 subject uni-coronal dataset, and a 25 subject metopic dataset. Each affected skull dataset was run against the same 34 unaffected skull dataset. To compare the effectiveness in distinguishing each affected group from controls, the above-described features were tested, both individually and in combination.

Table I gives the results of trying each of the four features individually. Column 1 shows the accuracy for the single-valued Compare to Circle (cmp2Circle) feature. Column 2 shows the accuracy for the single-valued Symmetry (symmetry) feature. Column 3 shows the results for the Angle feature (angleFnB) taken from 360 positions on the front and the back of the skull. Column 4 gives the accuracy for the Radius Distance feature (distFnB) taken from 360 positions on the front and the back of the skull. In both tables, #features refers to the total number of aggregate and low-level features used in that column.

TABLE I
ACCURACY WITH STANDARD DEVIATION OF USING EACH DESCRIPTOR (COLUMN) INDIVIDUALLY TO DISTINGUISH EACH AFFECTED SKULL DATASET (ROW) FROM 34 UNAFFECTED SKULLS.

	cmp2Circle	symmetry	angleFnB	distFnB
#features	1	1	360	360
Sagittal	94.50 (4.46)	67.54 (5.05)	97.22 (3.93)	95.06 (4.79)
Uni-coronal	73.08 (10.28)	91.15 (5.72)	89.56 (9.28)	86.65 (7.57)
Metopic	57.58 (1.60)	57.58 (1.60)	99.17 (2.64)	91.59 (8.79)

In Table II, column 1, (c-s) contains accuracy results using both comp2Circle and symmetry. Column 2 shows accuracy for the combination of these two features plus all the angle features (c-s + angleFnB). Column 3 contains the accuracy for the first two features plus all the distance features (c-s + distFnB). Column 4 shows the accuracy for all of the features (all). The total of all features is 722.

TABLE II
ACCURACY WITH STANDARD DEVIATION OF USING EACH DESCRIPTOR (COLUMN) COLLECTIVELY TO DISTINGUISH EACH AFFECTED SKULL DATASET (ROW) FROM 34 UNAFFECTED SKULLS.

	c-s	c-s + angleFnB	c-s + distFnB	all
#features	2	362	362	722
Sagittal	96.70 (3.87)	97.22 (3.93)	95.61 (4.29)	95.58 (4.38)
Uni-coronal	88.74 (6.58)	91.04 (7.54)	92.58 (5.99)	89.51 (10.13)
Metopic	57.58 (1.60)	99.17 (2.64)	91.59 (8.79)	99.17 (2.64)

In Table III, an additional experiment was performed in order to compare with Yang's results. Here, 3-fold cross validation with classifiers SMO and logistic regression were used in order to perform a direct comparison. The results demonstrated that the descriptor cmp2Circle is highly effective for sagittal detection, symmetry for uni-coronal, and angleFnB for most cases. Overall, the accuracy observed was higher in this system than in Yang's, particularly when all the descriptors were used together.

TABLE III
ACCURACY OF COMPARISON TO PREVIOUS RESULTS [9]. C IS CORONAL. M IS METOPIC. S IS SAGITTAL.

		C vs M	M vs S	S vs C	Three-Classes
Yang	C lasso	95.71	95.71	94.29	92.86
	F lasso	94.29	94.29	95.71	81.43
	L_1	92.86	95	93.57	91.43
	Log	86.43	86.43	76.07	90
all	SMO	99.67	99.64	98.89	99.2
	Log	96.55	96.34	100	-
angleFnB	SMO	100	100	100	100
	Log	98.28	96.34	100	97.39
distFnB	SMO	93.1	98.78	98.89	94.78
	Log	82.76	96.34	97.78	94.78
symmetry	SMO	87.93	69.51	93.33	73.04
	Log	91.38	70.73	93.33	73.91
cmp2Circle	SMO	81.03	93.9	100	82.61
	Log	79.31	93.9	100	86.96

VI. DISCUSSIONS AND CONCLUSIONS

This work was carried out to improve on prior work in which 1) no control data was available, 2) poor resolution, noise, missing slices, and other imperfections in the CT data eliminated many scans from use, and 3) the quantification measure was based on the mathematics of the classification method, not on an intuitive measure of shape. This work has a control set, is able to solve the imperfect data problem for many CT scans, and provides both a simple projection technique and several intuitive shape measures as part of a general platform.

By applying this framework on a CT surface mesh, our system can distinguish affected skulls from the unaffected ones. As shown in Table II, the two single-valued features (cmp2Circle and symmetry) plus the vector feature of 360 angle (angleFnB) achieves accuracies of 97.22%, 91.04% and 99.17% on the classification tasks of sagittal, unilateral coronal, and metopic vs control, respectively. Furthermore, as shown in Table III, when all features are used, accuracies reach 99.67%, 99.64%, 98.89% and 99.2% in four cases, respectively. These results show clear improvement over previous work [9].

Note that the angle descriptor (angleFnB) gave very high accuracies both in our own experiments of affected vs. control and on the comparison experiments with Yang's work, which had no controls and included classifications of pairs of classes and a 3-way class comparison. The accuracy of this feature in the latter comparisons with the SMO classifier was particularly high, 100% in all four cases. Since we are using cross-validation, we do not suspect overtraining. Instead, we believe that this is just a much easier task than distinguishing affected skulls from controls. The three abnormal classes are very different from one another. The SMO is a very powerful classifier, and it was able to learn to fully separate these classes on the amount of data we possess. On the more difficult task of distinguishing affected from controls, above 99% accuracy was only achieved on the metopic vs. control task and required the angleFnB feature.

We also note that the cmp2Circle descriptor gave very high accuracies to cases that involved sagittal synostosis on our own experiments of sagittal vs. control and on the comparison experiments with previous work. Similarly, the symmetry descriptor gave very high accuracies to cases that involved unilateral coronal synostosis on our own experiments of uni-coronal vs. control and on the comparison experiments with previous work. The *symmetry* descriptor can assess and determine which side of an unilateral coronal synostosis skull has the affected suture. In this experiment, the algorithm correctly predicted the affected sides 94% of the total uni-coronal synostosis cases.

Classification is not our final goal; it merely allows us to develop and judge shape features to be used for quantification. The results from our experiments are very promising not just for this classification experiment but for future work in assessing the severity of a skull's deformation caused by craniosynostosis and measuring the change effects from corrective surgery.

ACKNOWLEDGMENT

This research was supported by NIH/NIDCR under grant number U01 DE 020050 (Dr. Shapiro) and grant number R01 DE 13813 (Dr. Speltz).

REFERENCES

[1] B. Slater, K. Lenton, M. Kwan, D. Gupta, D. Wan, and M. Logaker, "Cranial sutures: a brief review," *Plast. Reconstr. Surg.*, vol. 121, no. 4, pp. 170e–178e, April 2008.

[2] J. Panchal and V. Uttchin, "Management of craniosynostosis," *Plast. Reconstr. Surg.*, vol. 111, no. 6, pp. 2032–48, May 2003.

[3] D. Gault, D. Renier, D. Marchac, and B. Jones, "Intracranial pressure and intracranial volume in children with craniosynostosis," *Plast. Reconstr. Surg.*, vol. 90, no. 3, pp. 377–81, September 1992.

[4] S. Ruiz-Correa, R. Sze, H. Lin, L. Shapiro, M. Speltz, and M. Cunningham, "Classifying craniosynostosis deformations by skull shape imaging," *18th IEEE Symposium on Computer-Based Medical Systems*, pp. 335–340, 2005.

[5] H. J. Lin, S. Ruiz-Correa, R. W. Sze, M. L. Cunningham, M. Speltz, A. V. Hing, and L. G. Shapiro, "Efficient symbolic signatures for classifying craniosynostosis skull deformities," *Proceedings of the Workshop on Computer Vision for Biomedical Image Applications*, pp. 302–313, October 2005.

[6] I. Atomsukarto, L. Shapiro, J. Starr, C. Heike, B. Collett, M. Cunningham, and M. Speltz, "3d head shape quantification for infants with and without deformational plagiocephaly," in *Cleft Palate Craniofac J.*, vol. 47(4), 2010, pp. 368–377.

[7] S. Lele and J. Richtsmeier, "An invariant approach to the statistical analysis of shapes," in *New York: Chapman and Hall/ CRC*, 2001.

[8] S. Ruiz-Correa, D. Gatica-Perez, H. Lin, and L. Shapiro, "A bayesian hierarchical model for classifying craniofacial malformations from ct imaging," in *30th Annual International IEEE EMBS conference*, 2008.

[9] S. Yang, L. Shapiro, M. Cunningham, M. Speltz, and S. Lee, "Classification and feature selection for craniosynostosis," in *ACM-BCB*, 2011.

[10] L. Massimi and M. Caldarelli, "Isolated sagittal cranosynostosis: definition, classification and surgical indications," in *Childs Nerv Syst*, vol. 28, 2012, pp. 1311–1317.